



Millisecond self-heating and quenching synthesis of Fe/carbon nanocomposite for superior reductive remediation

Liming Sun^a, Xuan Wu^a, Yubing Jiao^b, Chao Jia^a, Tao Teng^a, Litao Lin^a, Fengbo Yu^a, Zhelin He^a, Jie Gao^a, Shuwen Yan^a, Guosheng Shi^c, Zhiyong Jason Ren^d, Jinguang Yang^{b,*}, Shicheng Zhang^{a,e,**}, Xiangdong Zhu^{a,f,***}

^a Shanghai Technical Service Platform for Pollution Control and Resource Utilization of Organic Wastes, Shanghai Key Laboratory of Atmospheric Particle Pollution and Prevention (LAP3), Department of Environmental Science and Engineering, Fudan University, Shanghai 200092, China

^b Tobacco Research Institute of Chinese Academy of Agricultural Sciences, Qingdao 266000, China

^c State Key Laboratory Advanced Special Steel, Shanghai Applied Radiation Institute, Shanghai University, Shanghai 200444, China

^d Department of Civil and Environmental Engineering and Andlinger Center for Energy and the Environment, Princeton University, Princeton NJ 08544, United States

^e Shanghai Institute of Pollution Control and Ecological Security, Shanghai 200092, China

^f State Environmental Protection Engineering Center for Urban Soil Contamination Control and Remediation, Shanghai Academy of Environmental Sciences, Shanghai 200233, China



ARTICLE INFO

Keywords:

Fe⁰-based nanomaterials
Flash Joule heating
Reduction
Oxide shell-free
Environmental remediation

ABSTRACT

Fe⁰-based nanomaterials are extensively applied in environmental remediation, but their passivated oxide shell restricts deep application. However, efforts aimed at revitalizing Fe-oxide shells have shown limited success. Here, we report a “faster win fast” approach by preferential carbon layer deposition in milliseconds to block Fe-oxide shell growth via carbon-assisted flash Joule heating (C-FJH) reaction. C-FJH induced ultra-high temperature and electric shock promoted reductive Fe formation and subsequently melted to a phase-fusional heterostructure (Fe⁰/FeCl₂). Therefore, theoretical calculation confirmed that electron delocalization effect of derived heterostructure promoted electron transfer. Synchronously, rapid self-heating/quenching rate (~10² K/ms) realized a thin aromatic-carbon layer deposition to sustain both high stability and activity of reductive Fe. The channels of thin aromatic-carbon layer favored inward diffusion of pollutants, which facilitated the subsequent reduction. Accordingly, derived heterostructure and carbon layer jointly contributed to the boosted removal of multiple pollutants (including metal oxyanions, perfluorinated compounds, and disinfection by-products).

1. Introduction

Seminal studies on Fe⁰-based nanomaterials have made remarkable strides in environmental remediation because of the strong reducibility and environmental benignity of these materials [1–3]. However, to prevent self-overoxidation, Fe⁰-based materials carry a thick and passive Fe-oxide shell structure, thus deteriorating Fe⁰ reactivity by blocking inward mass transport and outward electron transfer [4,5]. To overcome the low reactivity of Fe⁰, numerous investigators endeavored to revitalize the oxide shell of Fe⁰. For instance, carbon-based material can be employed as a carrier to improve the dispersion and surface area of Fe⁰-based materials, thereby improving the enrichment/adsorption

performance of pollutants [6,7]. Furthermore, nano-cracks can be opened on the dense Fe-oxide shell structure through the embrittlement effect of liquid nitrogen or Kirkendall effect of phosphorylation [5,8]. Although these methods based on oxide shell revolution can enhance Fe⁰ activity to some degree, the rapid re-formation of the Fe-oxide shell compromises again the Fe⁰ reactivity [7,8]. Therefore, improving the long-term reactivity of Fe⁰-based nanomaterials still are a bottleneck [9].

In essence, a dense Fe-oxide shell structure is derived from rapid self-oxidation of Fe⁰ within minutes [10]. Therefore, we proposed a new “faster win fast” strategy to inhibit Fe-oxide shell growth. In this method, a “thin skin” faster deposited on the surface of Fe⁰ within

* Corresponding author.

** Corresponding authors at: Shanghai Technical Service Platform for Pollution Control and Resource Utilization of Organic Wastes, Shanghai Key Laboratory of Atmospheric Particle Pollution and Prevention (LAP3), Department of Environmental Science and Engineering, Fudan University, Shanghai 200092, China.

E-mail addresses: yangjinguang@caas.cn (J. Yang), zhangsc@fudan.edu.cn (S. Zhang), zxdjewett@fudan.edu.cn (X. Zhu).

milliseconds. Synchronously, this new skin should guarantee to not inhibit Fe^0 activity. Highly aromatic carbon typically has a large number of adsorption sites that favor the diffusion of pollutants [11,12], thus we imagine carbon layer can cooperate with Fe^0 to synergistically boost the reduction performance [7,13]. Opportunely, an emerging carbon-assisted flash Joule heating (C-FJH) technology can accomplish the aforementioned hypothesis [14,15]. Firstly, the C-FJH reaction induced ultra-high temperature (> 3000 K) and electric shock can promote the crack chemical bond of Fe-containing precursor to form reductive Fe components such as Fe^0 and Fe^{2+} [14]. At this temperature and during the C-FJH process, the rapid self-heating/quenching rate (~ 4000 K, $\sim 10^2$ K/ms) could ensure the volatiles derived from carbon substrate decomposition instantly deposit on the surface of Fe component within milliseconds [14]. Therein, the rapid self-heating/quenching process can be realized by programmed control reaction time (millisecond level) and input current. In addition, C-FJH induced thin aromatic-carbon layer should have a similar function to graphene in protecting reductive Fe components from oxidation [16, 17].

Additionally, C-FJH may confer multiple benefits. For example, the C-FJH reaction induced ultra-high temperature can pass the boiling point of metallic elements, resulting in metallic components present in liquid and interfusion forms. Thus, reductive bi-components (Fe^0 and Fe^{2+}) can fuse to form a phase-fusional heterostructure. Accordingly, the compositional flexibility of phase-fusional heterostructures could reinforce the ability of atomic orbital hybridization to improve the reductive capacity via electron delocalization effect [18,19]. Moreover, rapid quenching rates can hinder metal aggregation, ultimately resulting in highly-reactive metals with minor sizes that further enhance the material reactivity [20,21]. Undoubtedly, the C-FJH reaction can realize a “three birds with one stone” material characterized by oxide shell-free, partial phase-fusional heterostructure, and nano-size, thus opening a new era for reductive Fe-based nanomaterials.

In this work, we report a customized C-FJH process to synthesize oxide shell-free of Fe/carbon nanocomposite. We compared the functions and performance of Fe^0 -based materials produced using conventional $\text{NaBH}_4\text{-R}$ (NaBH_4 reduction) and $\text{H}_2\text{-R}$ (H_2 reduction) methods. As a proof-of-concept, multiple pollutants including perfluorooctane sulfonate (PFOS), perfluorooctanoic acid (PFOA), Cr(VI), Sb(V), and dichloroacetic acid (DCAA) were tested. We also expanded C-FJH technology to synthesize oxide shell-free of Cu or Ag/carbon nanocomposite as virus-inactivating agents for pepper mild mottle virus (PMMoV).

2. Experimental

2.1. Synthesis of reductive Fe /carbon nanocomposite by C-FJH reaction

A homemade C-FJH device was utilized to synthesize a robust Fe/carbon nanocomposite. Briefly, hydrochar and metallic salt with the same mass were uniformly mixed in anhydrous ethanol by oscillation and then suspended in a 60 °C vacuum oven to dry. Next, 10 wt% carbon black (conductive additive) was mixed with the dried solid mentioned above for C-FJH treatment. Finally, 0.1 g of the mixture was put into a quartz tube (tube thickness: 2 mm, inner diameter: 6 mm, length: 45 mm) and compressed with copper electrodes to minimize the sample resistance to $\sim 100 \Omega$. Then, a gentle vacuum was maintained during the reaction and purged with nitrogen to avoid sample oxidation. Finally, Fe/carbon nanocomposites were synthesized by adjusting C-FJH pulse voltage. A 50 ms duration time and 150–250 V pulse voltage were chosen as the flash Joule heating condition in this work. The preparation procedure for Cu or Ag/carbon nanocomposite is the same as above. More details can be found in the [Supporting information](#).

2.2. Characterization of reductive Fe/carbon nanocomposite

The heterostructure-Fe was demonstrated by high-resolution electron microscopy (HR-TEM). HR-TEM equipped with energy dispersive X-ray spectrometry (EDX) and high-angle annular dark-field (HAADF) images were performed to analyze elemental distributions and surface morphology. The distribution of Fe/carbon composite size was obtained using Nano Measurer 1.2 software to analyze TEM images of at least 100 particles. The composition and structure information of the as-prepared sample was analyzed by electron energy-loss spectroscopy (EELS) and X-ray absorption fine structure (XAFS). The free corrosion potentials and the charge transfer resistance was determined by Tafel and Electrochemical impedance spectroscopy (EIS) measurement, respectively. More details can be found in the [Supporting information](#).

3. Results and discussion

3.1. C-FJH advantages on reductive Fe/carbon nanocomposite fabrication

The C-FJH technology was compared with conventional chemical reduction ($\text{NaBH}_4\text{-R}$ and $\text{H}_2\text{-R}$) on fabricating reductive Fe/carbon nanocomposites. To initiate the C-FJH reaction, the mixture of FeCl_3 (precursor of reductive component), hydrochar (heating element), and carbon black (conductor) was compacted by two copper electrodes and then powered by a pulse voltage (Fig. 1a, Fig. S1). Accordingly, variable transient current-induced Joule heating resulted in an instantaneous temperature increase to ~ 4000 K (Fig. 1b, Fig. S2), as clearly seen by the dazzling light (Fig. 1c). Tuning the applied electrical pulse may affect the performance of the as-prepared reductive materials. The ultra-high temperature, electric shock, and rapid quenching rate are important features of the C-FJH reaction and may endow the as-prepared material with a carbon-encased phase-separated heterostructure or alloy structure (Fig. 1d) [14,22,23]. Regarding the fact that the Fe-oxide shell of Fe^0 can significantly hinder mass transport and electron transfer, thus decreasing the reactivity of Fe^0 (Fig. 1e) [24]. Accordingly, we predicted that the C-FJH-derived sample features a unique structure with an unprecedented reductive capacity (Fig. 1f), as confirmed by its high efficiencies ($> 90\%$) for removing multiple pollutants including PFOS, PFOA, Sb(V), Cr(VI), and DCAA (Fig. 1g). This view is further verified by comparing with other reported reductive capacities of Fe^0 -based materials (Fig. 1h) [5,8,9,25–28].

The role of carbon substrate (hydrochar) in fabricating reductive Fe/carbon nanocomposite by C-FJH reaction was further investigated. As shown in Fig. 1i, the C-FJH reaction was not initiated even when a high voltage was applied to FeCl_3 alone, as confirmed by the power and darkness of the as-prepared sample. Contrarily, the C-FJH reaction proceeded with the assistance of a carbon substrate because sufficient Joule heat was provided from the hydrochar via the Joule heating effect. Thus, carbon substrate for the C-FJH reaction is indispensable when fabricating reductive materials, as confirmed by the Cr(VI) removal results (Figs. S3–4).

Herein, taking “forever chemicals” PFOA and easily reduced Cr(VI) as probe indicators [29], we evaluated the reductive capacity of the as-prepared material. Compared to $\text{H}_2\text{-R}$ and $\text{NaBH}_4\text{-R}$ methods, C-FJH treatment significantly improved PFOA or Cr(VI) removal rate by more than 2.7 or 2.8-fold, respectively (Fig. 1j, Fig. S5–6). Clearly, the pollutants removal capacity of the C-FJH-derived sample was much higher than that of $\text{H}_2\text{-R}$ - and $\text{NaBH}_4\text{-R}$ -derived samples (Fig. S7), implying the highly reactive Fe of the C-FJH-derived sample (Fig. S8). In addition, the adsorption effect of the carbon substrate on pollutants removal was minor, indicating that the carbon substrate only provides adsorption sites in pollutants removal (Fig. S9). A previous study showed that surface area of material can influence the pollutants removal performance [30], so we calculated the surface-area-normalized PFOA and Cr(VI) removal rate constant k' . Compared to the $\text{H}_2\text{-R}$ - and

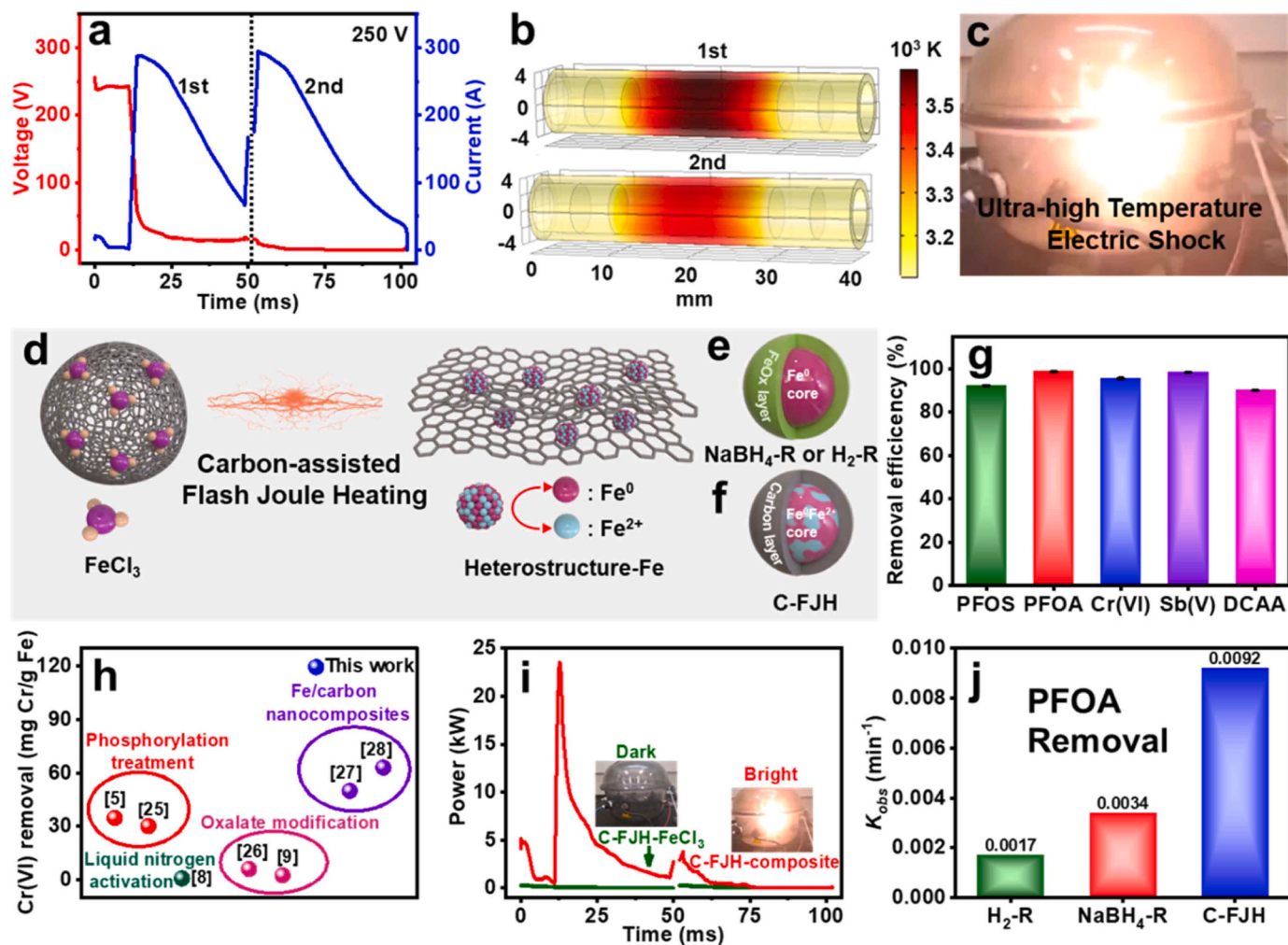


Fig. 1. Synthesis of reductive Fe/carbon nanocomposites and their performance in Cr(VI) removal. (a) Recorded current and voltage in carbon-assisted flash Joule heating (C-FJH) process. (b) 3D mapping temperature field simulation under C-FJH via COMSOL Multiphysics software. (c) Real-time photos of sample during the C-FJH process. (d) Schematic diagram for mechanism of reductive Fe/carbon nanocomposite preparation. (e) Core-shell structure of Fe^0 obtained using traditional preparation procedures. (f) Reductive Fe/carbon nanocomposite prepared using the C-FJH reaction. (g) Removal efficiencies of PFOS, PFOA, Cr(VI), Sb(V), and DCAA with Fe/carbon composite prepared by C-FJH. (h) The Cr(VI) removal capacity of reductive Fe was compared with reported reduction materials. (i) Power generated in C-FJH reaction with only FeCl_3 or a mixture of hydrochar and FeCl_3 precursor. (j) Comparison of apparent PFOA removal rate constant k_{obs} of different Fe/carbon composites prepared by C-FJH and conventional $\text{NaBH}_4\text{-R}$ or $\text{H}_2\text{-R}$ methods. (Experimental parameters: [PFOS] or [PFOA] = 0.1 mg L^{-1} , reaction time = 1 h, reaction time = 2 h, dose of sample, 1 g L^{-1} ; [Cr(VI)] = 10 mg L^{-1} , reaction time = 1 h, dose of sample, 1 g L^{-1} ; [Sb(V)] = 5.11 mg L^{-1} , reaction time = 24 h, dose of sample = 2.5 g L^{-1} ; [DCAA] = 10.66 mg L^{-1} , reaction time = 72 h, dose of sample = 3 g L^{-1} , initial pH = 4.0; temperature, 25°C).

NaBH₄-R-derived samples, the C-FJH-derived sample had a higher k' value but a relatively small surface area. This result strongly excluded the contribution of surface area enhancement to pollutant removal (Fig. S10).

3.2. C-FJH induced oxide shell-free and phase-fusional heterostructure

To understand the improved reactivity of the C-FJH-derived sample, we performed various structural analyses of different Fe/carbon composites. Traditional NaBH₄-R and H₂-R methods for producing Fe^0 were composed of necklace-like or spherical aggregate with a distinct core-shell structure [5,31], as confirmed by the bright inner core and dim outer shell of HAADF images (Fig. 2a, b). Moreover, Fe + C + O overlapped elemental mapping of EDX results suggested that the Fe core was encapsulated by a dense Fe-oxide shell that was 7.2 and 13.5 nm thick in the NaBH₄-R- and H₂-R-derived samples, respectively. Theoretically, the encrusted Fe-oxide shell can hinder electron transfer from the Fe core to Fe-oxide shell [32], thereby inhibiting the reductive efficiency. Accordingly, the H₂-R-derived sample with a thicker oxide shell

exhibited an inferior reductive capacity (Fig. S7). Notably, despite numerous efforts attempted to reform the oxide shell of Fe^0 (refs. [5,8, 33]), success has been very limited.

Intriguingly, the Fe sphere of C-FJH-derived sample showed no significant color difference, as clearly confirmed by HAADF images (Fig. 2c), strongly implying a lack of the Fe-oxide shell. Subsequently, the scattered distribution of O elements and the absence of dense surface rings confirmed this result, as demonstrated in O and overlapped Fe + C + O elemental mapping. Undoubtedly, the lack of oxide shells decreases the stability of Fe^0 -based materials [34,35]. Therefore, intrinsically maintaining the stability and activity of materials is challenging. Importantly, HR-TEM images strongly confirmed that the inner Fe core of the C-FJH-derived sample was tightly encapsulated by a $\sim 2.5 \text{ nm}$ carbon layer (Fig. 2d). Owing to the rapid self-heating/quenching rate during the C-FJH process, the decomposition products of the carbon substrate were instantly deposited on the surface of the Fe component. Additionally, the carbon layer formation rate was overwhelmingly faster than that of oxide shell, thus intensively hindering the oxide shell formation. In general, the coating of the stabilizer on the surface of Fe^0 will

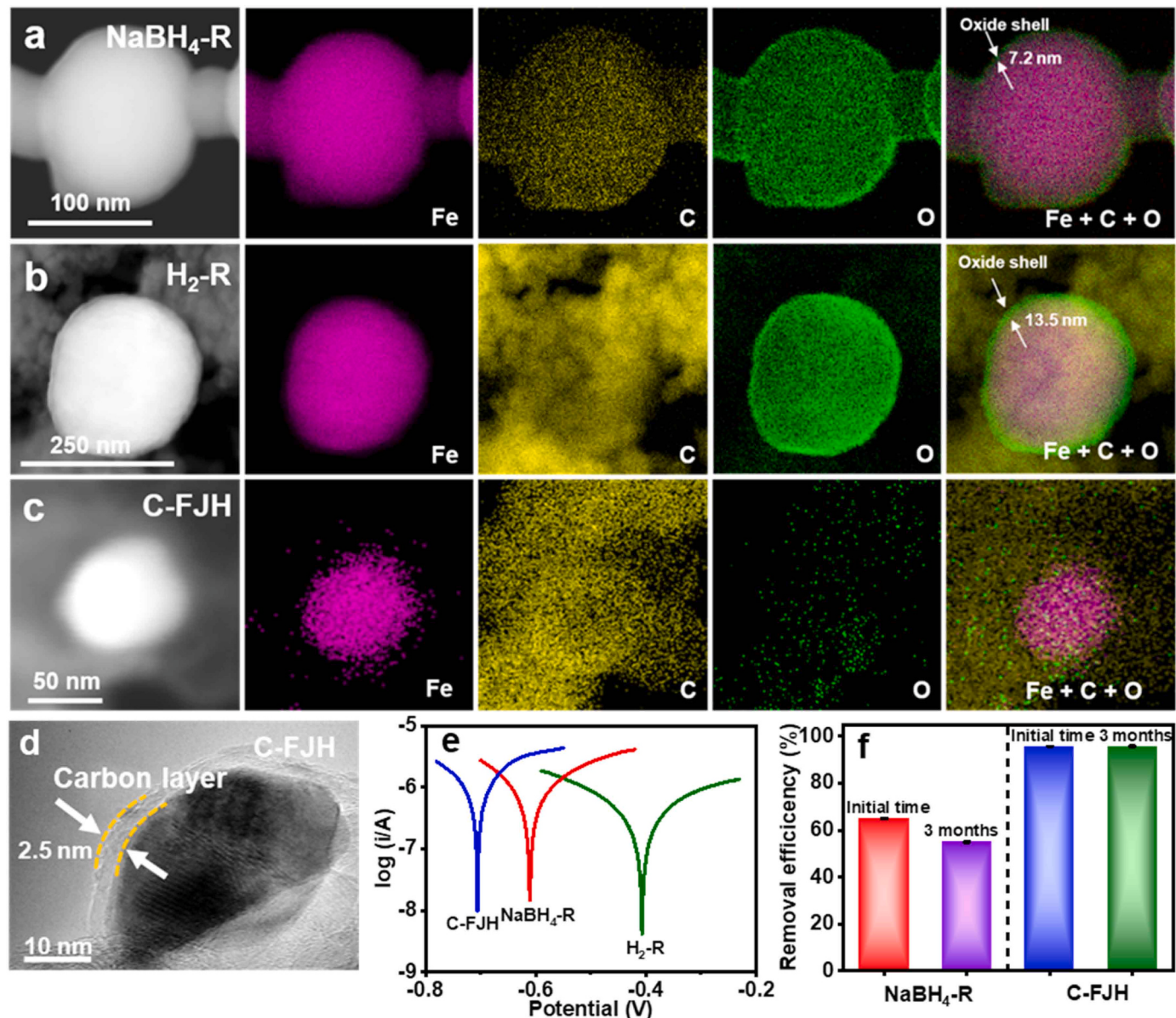


Fig. 2. Morphology and surface chemical property analysis. (a) High-angle annular dark-field (HAADF) images of $\text{NaBH}_4\text{-R}$ -derived sample and corresponding energy-dispersive X-ray (EDX) elemental mapping of Fe, C, O, and their overlapped images. (b) HAADF images of $\text{H}_2\text{-R}$ -derived sample and corresponding EDX elemental mapping of Fe, C, O, and their overlapped images. (c) HAADF images of C-FJH-derived sample and corresponding EDX elemental mapping of Fe, C, O, and their overlapped images. (d) High-resolution transmission electron microscopy (HR-TEM) images of C-FJH-derived sample. (e) Tafel curves of Fe/carbon composite by C-FJH and conventional $\text{NaBH}_4\text{-R}$ or $\text{H}_2\text{-R}$ methods. (f) Stability analysis of $\text{NaBH}_4\text{-R}$ - and C-FJH-derived samples during Cr(VI) removal. (Samples exposed to air for 3 months) Note: To ensure the consistency of the samples, the same proportion of carbon black was added to the raw materials of the three as-prepared samples.

reduce the diffusion channel and block the active site, thus inhibiting the electron transfer of the Fe core to the pollutant [11]. Strikingly, the C-FJH-derived sample presented extraordinarily faster electron transfer, as this sample showed the most negative free corrosion potential (-0.706 V) (Fig. 2e, Fig. S11) [36,37]. In essence, the aromatic-carbon layer can certainly act as a citadel to protect Fe core from oxidation [36, 37]. The C-FJH-derived sample exhibited outstanding stability, as confirmed by high Cr(VI) removal reactivity even exposed to air for three months (Fig. 2f, Fig. S12).

Compared to the dense Fe core of $\text{NaBH}_4\text{-R}$ - and $\text{H}_2\text{-R}$ -derived samples, the Fe core was relatively sparse and formed numerous nanocracks in Fe elemental mapping of the C-FJH-derived sample (Fig. 2c). Electric shock induced by the C-FJH reaction breaks the magnetic and electrostatic forces within the particles, resulting in the formation of nanocracks. Undoubtedly, nano-cracks can facilitate interfacial electron/

mass diffusion [5].

Moreover, the C-FJH-derived sample showed the smallest average particle size because rapid heating/quenching inhibited metal agglomeration (Fig. S13), which can further increase the exposure of active sites in the sample [38,39]. Thus, the C-FJH reaction can loosen the Fe core and produce a nano-size effect. Obviously, the comprehensive effects in the C-FJH process changed both the bulk structure and surface construction of the Fe core.

From the X-ray diffraction (XRD) patterns in Fig. S14, $\alpha\text{-Fe}^0$ was the only Fe species in the $\text{NaBH}_4\text{-R}$ - and $\text{H}_2\text{-R}$ -derived samples, whereas $\gamma\text{-Fe}^0$ and FeCl_2 were the main Fe species in the C-FJH-derived sample. Obviously, the C-FJH reaction can induce specific structural changes in reductive materials, therefore, we applied electron energy-loss spectroscopy (EELS) and X-ray absorption fine structure (XAFS) to obtain the composition and structure information of the C-FJH-derived sample.

Firstly, HR-TEM images revealed the inner phase is $\gamma\text{-Fe}^0$ and FeCl_2 based on lattice spaces of 0.18 and 0.13 nm, respectively, indicating the formation of heterostructure-Fe (Fig. 3a) [40,41]. Furthermore, Fe^0 and Fe^{2+} were evenly distributed over the entire single particle, as confirmed by annular bright-field scanning (ABF) images and the corresponding EELS spectrum (Fig. 3b,c). These results further imply phase-fusional heterostructures formation, as ultra-high temperatures can crack the Fe-Cl bond and subsequently alloy the reductive components during the C-FJH process [14].

As reported previously, the dense Fe-oxide shell can hamper mass transport and electron transfer simultaneously [42]. Therefore, it is urgent to understand why substituting a carbon layer for an oxide shell still maintains the activity of the Fe/carbon nanocomposite. Given the removal process of organics is difficult to observe with an electron microscope. Herein, with Cr(VI) removal as a model reaction, the time-sequence structural evolution of individual Fe spheres was tracked through electron microscopy. After a 5-min reaction, Cr(VI) penetrated the carbon layer and scattered distribution in the inner Fe core of the C-FJH-derived sample, as indicated by the increase in Fe, C, and Cr elemental mapping (Fig. 3d). As the reaction progresses, Cr(VI) is completely distributed on the Fe core, as evidenced by Cr elemental mapping of the C-FJH-derived sample (Fig. 3d,e) [43]. Moreover, in the air atmosphere, the C-FJH-derived sample maintained high-activity because of the oxygen resistance of the carbon layer (Fig. S15).

To further probe the oxidation states and coordination environment for C-FJH-derived material, X-ray absorption near-edge structure (XANES) and extended X-ray absorption fine structure (EXAFS) of Fe K-edges were conducted. Fig. 4a presents the k^3 -weighted Fourier transform (FT)-EXAFS spectra of the existence of a Fe-Fe bond at a peak of

2.50 Å, and the radical distance of Fe-Cl decreased to 2.17 Å after C-FJH treatment (Table S1). The Cl coordination number of Fe in the C-FJH-derived sample was reduced from 6 to 5.6, compared to FeCl_2 standard. Thus, partial cracking of the Fe-Cl bond and Cl volatilization occurred at ultra-high temperatures during the C-FJH process to produce Fe^0 that filled the Cl position. This result further confirms the occurrence of partial phase fusion, which agrees with the EELS results. Moreover, XANES spectra revealed that the rising edge of the C-FJH-derived sample was situated between Fe foil and FeCl_2 , suggesting that the Fe atoms were in an intermediate state between Fe^0 and Fe^{2+} (Fig. 4b). The oxidation state of Fe was +1.2 from the Fe K-edge XANES via linear fitting between the valence states of Fe and first inflection point of the derivative spectrum [44], supporting the coexistence of Fe^0 and FeCl_2 (Fig. 4c). X-ray photoelectron spectroscopy (XPS) analysis further confirmed the existence of Fe^0 in the C-FJH-derived sample resulting from breakage of the Fe-Cl bond during the C-FJH process (Fig. S16). The Wavelet transform (WT) also confirmed the existence of Fe-Cl and Fe-Fe coordination, compared to that of the standards (Fig. 4d). Accordingly, a fusion phase was formed after C-FJH treatment, and this unique $\text{Fe}^0/\text{FeCl}_2$ heterostructure may be the main reason for the enhanced reductive capacity.

Given the critical role of carbon structure in pollutant removal, it is essential to understand how the carbon substrate varies during the C-FJH process. As revealed by the C 1 s XPS spectrum, the abundance ratio of C=C to C-C was the largest in the C-FJH-derived sample, indicating a higher degree of aromatization (Fig. S17, Table S2) [45,46]. Subsequent Raman spectroscopy also confirmed this result (Fig. 4e, Table S2) [15]. The highly aromatic-carbon can promote the diffusion of pollutants via defective channel [11]. Furthermore, the electrochemical impedance

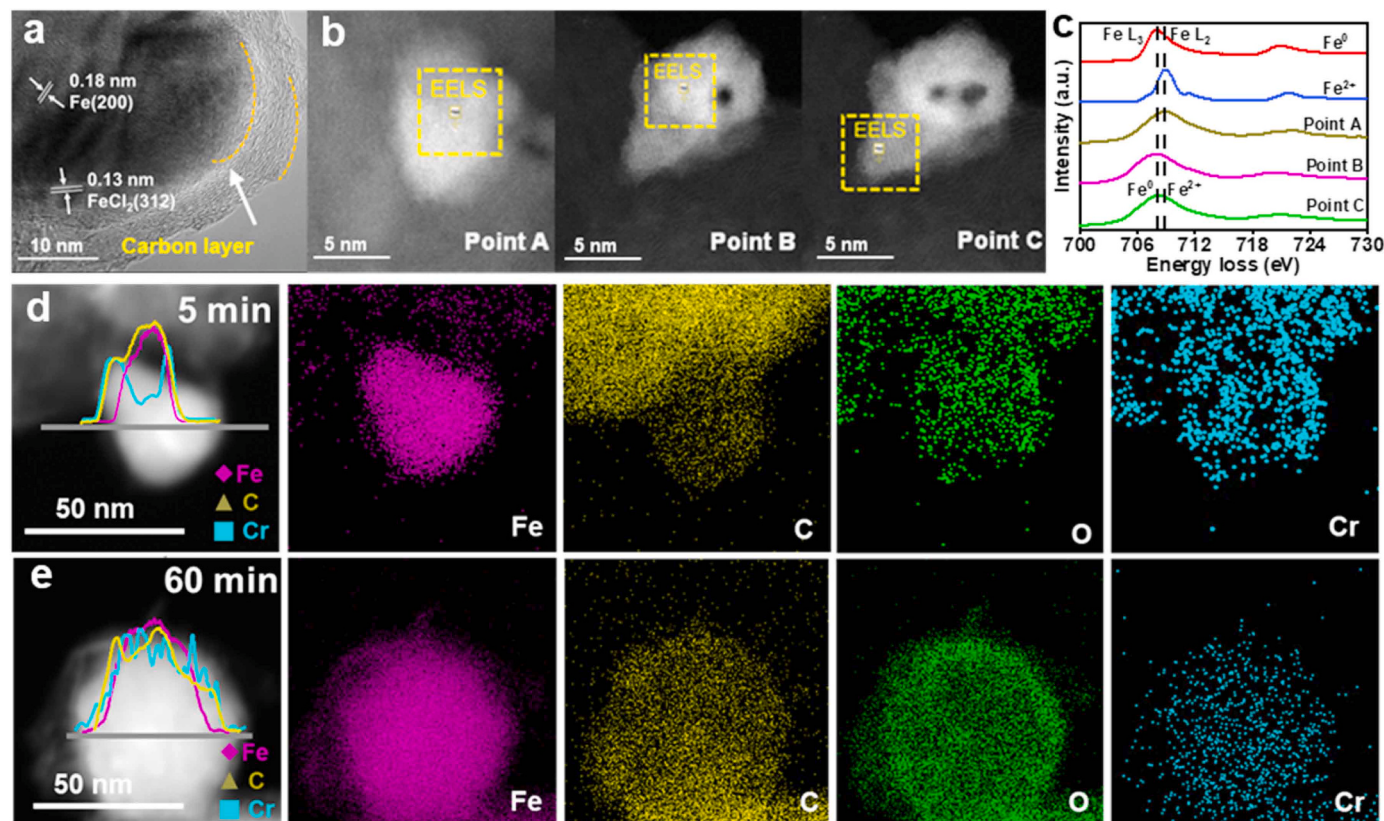


Fig. 3. Component analysis and structure evolution during Cr(VI) removal process. (a) HR-TEM images of the C-FJH-derived sample. (b) Annular bright-field scanning (ABF) images of the C-FJH-derived sample. (c) Fe L_3 edge positions of Fe^0 (708 eV) and Fe^{2+} (708.85 eV) for Fe species in the electron energy-loss spectroscopy (EELS) spectrum of the C-FJH-derived sample. (d) HAADF-STEM images of C-FJH-derived sample reacted with Cr(VI) for 5 min and the corresponding EDX elemental mapping of Fe, C, O, Cr. (e) HAADF-STEM images of C-FJH-derived sample reacted with Cr(VI) for 60 min and the corresponding EDX elemental mapping of Fe, C, O, Cr. Note: The removal process of organics is difficult to observe with electron microscopy, so Cr(VI) removal is selected as the model reaction.

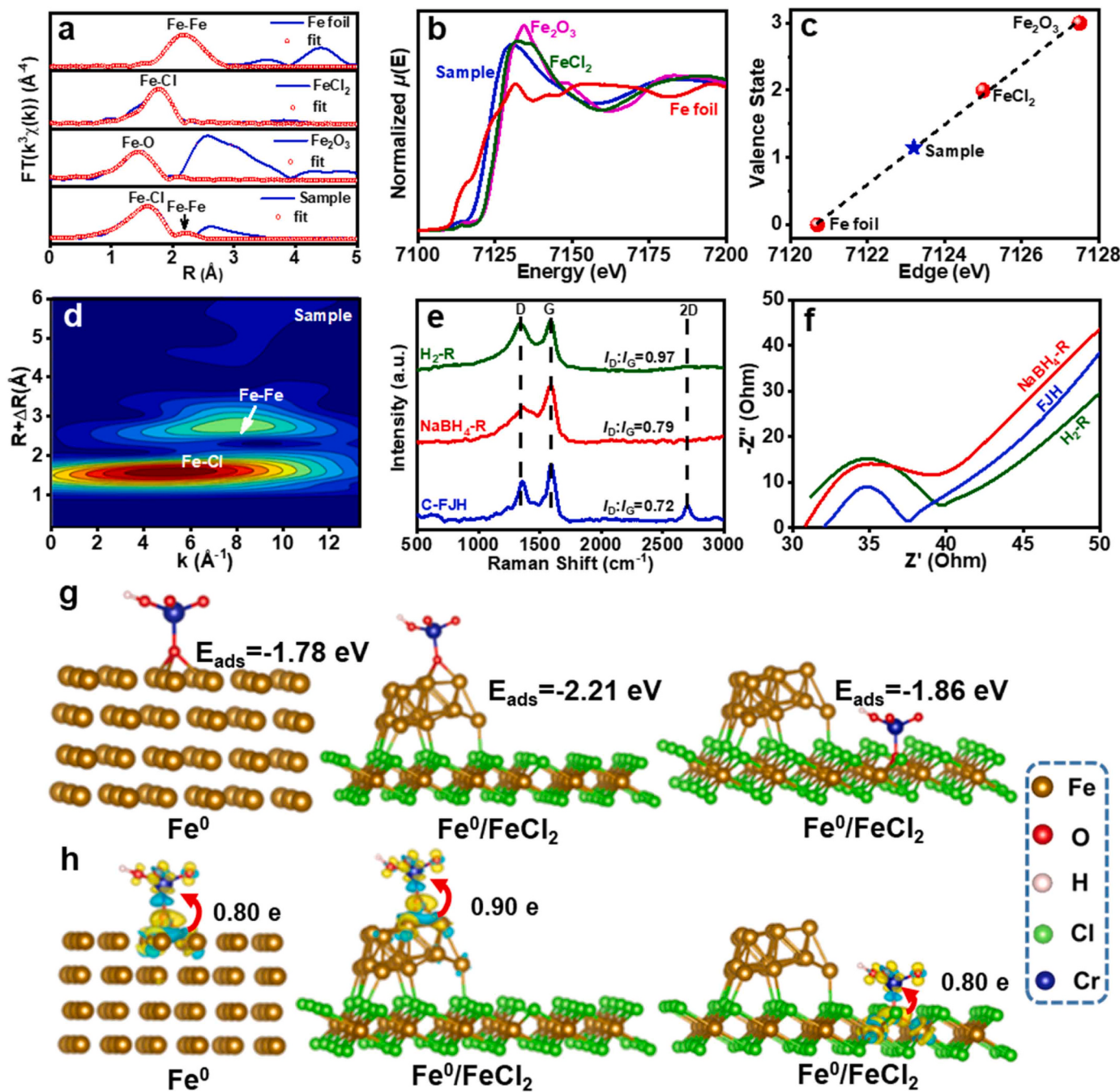


Fig. 4. Component analysis and reaction mechanism. (a) Extended X-ray absorption fine structure (EXAFS) fitting curves of Fe foil, FeCl₂, Fe₂O₃, and C-FJH-derived sample in R space. (b) Fe K-edge XANES spectra of C-FJH-derived sample. (c) XANES fitting valence of C-FJH-derived sample. (d) Wavelet transform (WT) analysis of C-FJH-derived sample. (e) Raman spectrum of the Fe/carbon composite prepared using C-FJH and conventional NaBH₄-R or H₂-R methods. (f) Electrochemical impedance spectroscopy (EIS) curves of the Fe/carbon nanocomposite prepared using C-FJH and conventional NaBH₄-R or H₂-R methods. (g) Density functional theory (DFT) calculation of HCrO₄ coordinated with Fe⁰ and Fe⁰/FeCl₂. (h) DFT calculation of charge-density difference in HCrO₄ adsorbed on Fe⁰ and Fe⁰/FeCl₂. The yellow and blue isosurfaces represent the charge accumulation and depletion region, respectively. Note: Models of Fe⁰ and the heterostructure Fe⁰/FeCl₂ were constructed to compare the contribution of active species, so no additional carbon layers were added to the models.

spectroscopy results confirmed the C-FJH-derived sample possessed the lowest charge transfer resistance, this contributes to electron transfer (Fig. 4f).

We further studied the effects of C-FJH power on the different Fe/carbon nanocomposites of reductive capacity. The C-FJH reaction becomes more violent as the applied pulse voltage increases, causing the reaction temperature to rise (Fig. 1a, Fig. S2, Fig. S18-19). It was found the pollutant removal efficiency increased from 73.1% to 95.6% with increasing the input power (Fig. S20-21), as evidenced by the faster

electron transport of the higher-power obtained sample (Fig. S22). Because the decomposition temperature of any metal salt is less than 3000 K [14], the strong C-FJH reaction induced by high power can promote cracking of the Fe-Cl bond to produce more reductive Fe. Furthermore, for different iron salt precursors, the Fe/carbon nanocomposite prepared using C-FJH technology exhibited excellent reduction performance (Fig. S23). The bond energy of Fe-Cl (351 KJ/mol) is lower than that of Fe-O (390.4 \pm 17.2 KJ/mol) [47], which can affect the reductive Fe component generated by the C-FJH process, and

ultimately affect the removal effect of pollutants. The subsequent Tafel results can support this inference (Fig. S24). Even at the same input voltage, different Fe precursors (ferric acetate and ferrous oxalate) samples derived from C-FJH can trigger varied Joule heating effects. Raising the current through the sample will cause a sharp rise in the temperature and power of the sample, which will undoubtedly promote the break of chemical bonds to form reductive components. However, excessive temperature will also accelerate the volatilization of metal elements (Fig. S25-27) [14,48]. Tuning the appropriate electrical parameters is the key to obtaining reductive components.

3.3. Reduction mechanism of Fe/carbon nanocomposite

Exemplified by Cr(VI) or PFOA removal, we explored the reduction mechanism of different Fe/carbon composites. Considering Fe(II) plays an indispensable role in pollutant removal [26], therefore, the contribution of Fe(II) to Cr(VI) or PFOA reduction was firstly investigated. The amount of Fe(II) released suggests that Fe(II) may participate in Cr(VI) reduction (Fig. S28a, b). As expected, Cr(VI) removal over $\text{H}_2\text{-R}$ - and $\text{NaBH}_4\text{-R}$ -derived samples were suppressed to a certain extent by addition of 1,10-phenanthroline, whereas Cr(VI) removal over the C-FJH-derived sample showed almost no change (Fig. S29). This contrast indicates that dissolved Fe(II) played a minor role in removing Cr(VI) from the C-FJH-derived sample. It should be noted that structural Fe(II) ($E_0 = -0.34$ to -0.65 V) is more reducible than aqueous Fe(II) ($E_0 = 0.77$ V) [23,49], thus favoring the Cr(VI) reduction. Assuming that all Fe^0 content (1.32 μmol) in the C-FJH-derived sample is involved in Cr(VI) reduction (Fig. S30), it can only reduce 15.2% of total Cr(VI). Thus, this result strongly supported the major active component is $\text{Fe}^0/\text{FeCl}_2$ heterostructure for Cr(VI) removal. Considering that Cr(VI) is easy to

reduce, we also tested the effect of $\text{Fe}(\text{II})$ on the PFOA removal. Surprisingly, the removal effect of PFOA was slightly suppressed by adding of 1,10-phenanthroline (Fig. S31). Therefore, $\text{Fe}^0/\text{FeCl}_2$ heterostructure can be the main reason for the reduction performance improvement.

Furthermore, we theoretically unraveled the role of heterostructure-Fe in enhancing the reduction performance. Fe^0 is used as the benchmark model, whereas some Fe atoms are placed on the FeCl_2 model to form a $\text{Fe}^0/\text{FeCl}_2$ heterostructure model. The theoretical calculation results presented that the calculated adsorption energy of Cr(VI) on the Fe^0 site or Fe^{2+} site of $\text{Fe}^0/\text{FeCl}_2$ heterostructure was -2.21 or -1.86 eV, respectively, obviously lower than that (-1.78 eV) of a single Fe^0 system (Fig. 4g, Fig. S32). These results support that Cr(VI) preferentially coordinates with the Fe^0 sites of the $\text{Fe}^0/\text{FeCl}_2$ heterostructure with lower adsorption energy, which can contribute to the enhanced Cr(VI) removal. Charge-density difference calculations revealed that Cr(VI) adsorbed on a single Fe^0 system accepts electrons from Fe^0 via a single-channel pathway. In contrast, Cr(VI) adsorbed on the $\text{Fe}^0/\text{FeCl}_2$ heterostructure captured electrons in diverse manners, as two types of Fe atoms can combine with Cr(VI). The difference in the electron transfer pathway resulted in a better electron-withdrawing ability of Cr(VI) on the $\text{Fe}^0/\text{FeCl}_2$ heterostructure surface, as reflected by its higher electron transport quantity (Fig. 4h). This is because the electron delocalization effect enabled more electrons to be transferred to the interface of Fe^0 and FeCl_2 , thus favoring the subsequent Cr(VI) reduction [9]. These results confirmed that the $\text{Fe}^0/\text{FeCl}_2$ heterostructure significantly improved reduction properties.

3.4. Expansion of C-FJH technology on Cu or Ag/carbon nanocomposite

Until now, obtaining non-oxidized Cu or Ag nanomaterials remains

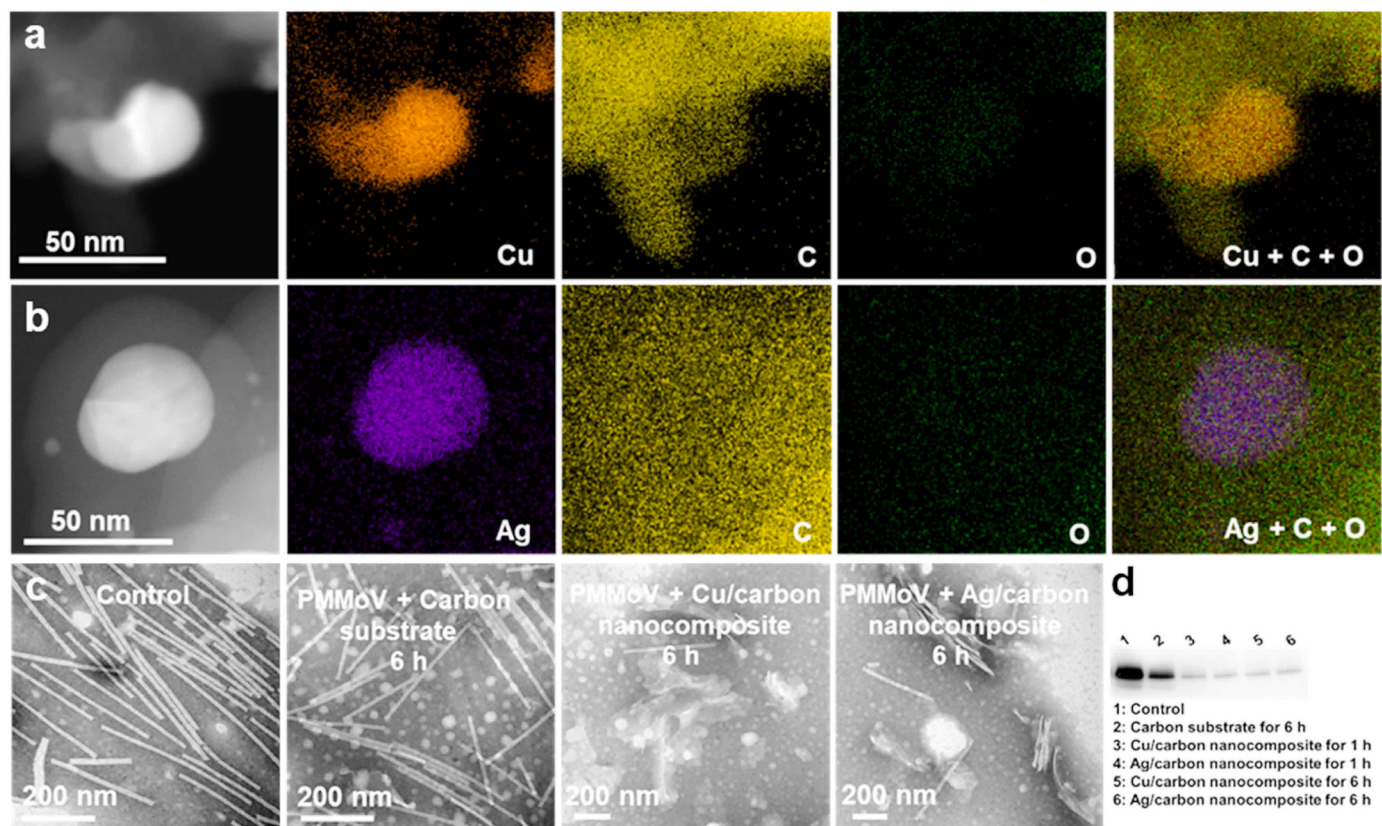


Fig. 5. Expanded application of C-FJH technology. (a) HAADF images of Cu/carbon nanocomposite and corresponding EDX elemental mapping of Cu, C, O, and their overlapped images. (b) HAADF images of Ag/carbon nanocomposite and corresponding EDX elemental mapping of Ag, C, O, and their overlapped images. (c) TEM images of pepper mild mottle virus (PMMoV) treated under different conditions as specified in the images. (d) Western blot analysis of PMMoV incubated with carbon substrate, Cu, or Ag/carbon nanocomposites for 1 or 6 h. (dose of sample = 3.5 g L⁻¹).

challenging [34,35]. To expand the utilization potential of C-FJH technology, we tested this process on preparing Cu or Ag/carbon nanocomposites. Both Cu and Ag/carbon nanocomposites prepared using C-FJH technology lack an obvious oxide shell, as evidenced by O elemental mapping and HAADF images (Fig. 5a,b). In benchmark experiments, both metal-based nanocomposites led to PMMoV fracture and even deformation *in vitro*, whereas PMMoV particles in the untreated group exhibited a baculiform shape and were evenly distributed (Fig. 5c). Besides TEM evidence, western blotting showed that the band corresponding to capsid protein faded away after Cu or Ag/carbon nanocomposites treatment, indicating the rapid loss of viral activity (Fig. 5d, Fig. S33, Table S3) [50,51]. Although the oxide shell is missing, the Cu or Ag/carbon nanocomposites can still maintain high-activity to directly injure PMMoV shell proteins. Therefore, Cu or Ag/carbon nanocomposites prepared by C-FJH technology show potential as virus-inactivating agents for PMMoV.

4. Conclusions

We report an innovative C-FJH process for fabricating a reductive Fe/carbon nanocomposite with excellent removal capacity and longevity. With such an approach, we synthesized materials with multiple benefits, featuring oxide shell-free, partial phase-fusional heterostructure, and nano-size. A highly aromatic-carbon layer derived from C-FJH favors inward diffusion of pollutants, which facilitated to the subsequent reduction. Theoretical calculations indicated that the C-FJH reaction induced phase-fusional $\text{Fe}^0/\text{FeCl}_2$ heterostructure captures more electrons for decontamination due to the electron delocalization effect. Moreover, the C-FJH-derived sample demonstrated versatility in removing multiple pollutants such as PFOS, PFOA, Sb(V), and DCAA. Importantly, C-FJH also successfully expanded on preparing Cu or Ag/carbon nanocomposites with oxide shell-free structures for high-efficiency virus inactivation. Therefore, C-FJH opens a vast space for synthesizing metal-based nanocomposites with great potential for practical application.

CRediT authorship contribution statement

Liming Sun: Conceptualization, Methodology, Investigation, Formal analysis, Data curation, Visualization, Writing – original draft. **Xuan Wu:** Visualization. **Yubing Jiao:** Resources, Investigation, Formal analysis. **Chao Jia:** Investigation. **Tao Teng:** Investigation. **Litao Lin:** Data curation, Visualization, Software. **Fengbo Yu:** Investigation. **Zhe-lin He:** Investigation. **Jie Gao:** Investigation. **Shuwen Yan:** Resources, Investigation, Formal analysis. **Guosheng Shi:** Writing – review & editing. **Zhiyong Jason Ren:** Writing – review & editing. **Jingguang Yang:** Funding acquisition, Resources, Writing – review & editing. **Shicheng Zhang:** Resources, Supervision, Writing – review & editing. **Xiangdong Zhu:** Conceptualization, Methodology, Resources, Supervision, Funding acquisition, Writing – review & editing.

Declaration of Competing Interest

The authors declare that they have no known competing financial interests or personal relationships that could have appeared to influence the work reported in this paper.

Data Availability

No data was used for the research described in the article.

Acknowledgments

This work was supported by the National Natural Science Foundation of China (No. 22276040), the special fund of State Environmental Protection Engineering Center for Urban Soil Contamination Control and

Remediation (USCR-202204), Major Green Prevention and Control Projects (110202101045 (LS-05)), and leading project of Bai Ma Future Food Research Institute (JBGS-2021-007). We thank the DFT calculations assisted by Shenzhen HUASUAN Technology Co., Ltd. We especially appreciate the XAFS measurements provided by Anhui Absorption Spectroscopy Analysis Instrument Co., Ltd.

Appendix A. Supporting information

Supplementary data associated with this article can be found in the online version at doi:10.1016/j.apcatb.2023.123361.

References

- [1] T. Pak, L.F.L. Luz Jr., T. Tosco, G.S.R. Costa, P.R.R. Rosa, N.L. Archilha, Pore-scale investigation of the use of reactive nanoparticles for *in situ* remediation of contaminated groundwater source, Proc. Natl. Acad. Sci. USA 117 (2020) 13366–13373.
- [2] J. Xu, A. Avellan, H. Li, X. Liu, V. Noel, Z. Lou, Y. Wang, R. Kaegi, G. Henkelman, G.V. Lowry, Sulfur loading and speciation control the hydrophobicity, electron transfer, reactivity, and selectivity of sulfidized nanoscale zerovalent iron, Adv. Mater. 32 (2020), e1906910.
- [3] Y. Liu, T. Wu, J.C. White, D. Lin, A new strategy using nanoscale zero-valent iron to simultaneously promote remediation and safe crop production in contaminated soil, Nat. Nanotechnol. 16 (2021) 197–205.
- [4] S. Bae, R.N. Collins, T.D. Waite, K. Hanna, Advances in surface passivation of nanoscale zerovalent Iron: a critical review, Environ. Sci. Technol. 52 (2018) 12010–12025.
- [5] L. Zhang, M. Li, H. Shang, H. Li, Y. Hong, C. Ling, K. Wei, B. Zhou, C. Mao, Z. Ai, Kirkendall effect boosts phosphorylated nZVI for efficient heavy metal wastewater treatment, Angew. Chem. Int. Ed. Engl. 60 (2021) 17115.
- [6] P. Fan, X. Zhang, H. Deng, X. Guan, Enhanced reduction of p-nitrophenol by zerovalent iron modified with carbon quantum dots, Appl. Catal. B Environ. 285 (2021), 119829.
- [7] H. Lv, H. Niu, X. Zhao, Y. Cai, F. Wu, Carbon zero-valent iron materials possessing high-content fine Fe^0 nanoparticles with enhanced microelectrolysis-Fenton-like catalytic performance for water purification, Appl. Catal. B Environ. 286 (2021), 119940.
- [8] Y. Hu, X. Peng, Z. Ai, F. Jia, L. Zhang, Liquid nitrogen activation of zero-valent iron and its enhanced Cr(VI) removal performance, Environ. Sci. Technol. 53 (2019) 8333–8341.
- [9] M. Liao, X. Wang, S. Cao, M. Li, X. Peng, L. Zhang, Oxalate modification dramatically promoted Cr(VI) removal with zero-valent iron, ACS Environ. Sci. Technol. Water 1 (2021) 2109–2118.
- [10] Y. Mu, F. Jia, Z. Ai, L. Zhang, Iron oxide shell mediated environmental remediation properties of nano zero-valent iron, Environ. Sci. Nano 4 (2017) 27–45.
- [11] W. Liang, G. Wang, C. Peng, J. Tan, J. Wan, P. Sun, Q. Li, X. Ji, Q. Zhang, Y. Wu, W. Zhang, Recent advances of carbon-based nano zero valent iron for heavy metals remediation in soil and water: a critical review, J. Hazard. Mater. 426 (2022), 127993.
- [12] C. Zhao, L. Meng, H. Chu, J.-F. Wang, T. Wang, Y. Ma, C.-C. Wang, Ultrafast degradation of emerging organic pollutants via activation of peroxyomonosulfate over $\text{Fe}_3\text{C}/\text{Fe}@\text{N-C-x}$: Singlet oxygen evolution and electron-transfer mechanisms, Appl. Catal. B Environ. 321 (2023), 122034.
- [13] K.M. Wyss, J.L. Beckham, W. Chen, D.X. Luong, P. Hundt, S. Raghuraman, R. Shahsavari, J.M. Tour, Converting plastic waste pyrolysis ash into flash graphene, Carbon 174 (2021) 430–438.
- [14] Y. Yao, Z. Huang, P. Xie, S.D. Lacey, R.J. Jacob, H. Xie, F. Chen, A. Nie, T. Pu, M. Rehwoldt, D. Yu, M.R. Zachariah, C. Wang, R. Shahbazian-Yassar, J. Li, L. Hu, Carbothermal shock synthesis of high-entropy-alloy nanoparticles, Science 359 (2018) 1489–1494.
- [15] D.X. Luong, K.V. Bets, W.A. Algozeel, M.G. Stanford, C. Kittrell, W. Chen, R. V. Salvatierra, M. Ren, E.A. McHugh, P.A. Advincula, Z. Wang, M. Bhatt, H. Guo, V. Mancevski, R. Shahsavari, B.I. Yakobson, J.M. Tour, Gram-scale bottom-up flash graphene synthesis, Nature 577 (2020) 647–651.
- [16] M. Song, L. Feng, P. Huo, M. Liu, C. Huang, F. Yan, Y.-q Lu, T. Xu, Versatile full-colour nanopainting enabled by a pixelated plasmonic metasurface, Nat. Nanotechnol. 18 (2022) 71–78.
- [17] F. Jiang, Y. Yao, B. Natarajan, C. Yang, T. Gao, H. Xie, Y. Wang, L. Xu, Y. Chen, J. Gilman, L. Cui, L. Hu, Ultrahigh-temperature conversion of biomass to highly conductive graphitic carbon, Carbon 144 (2019) 241–248.
- [18] Z. Huang, J.-X. Liang, D. Tang, Y. Chen, W. Qu, X. Hu, J. Chen, Y. Dong, D. Xu, D. Golberg, J. Li, X. Tang, Interplay between remote single-atom active sites triggers speedy catalytic oxidation, Chem. 8 (2022) 1–10.
- [19] Z.Y. Guo, Y. Si, W.Q. Xia, F. Wang, H.Q. Liu, C. Yang, W.J. Zhang, W.W. Li, Electron delocalization triggers nonradical Fenton-like catalysis over spinel oxides, Proc. Natl. Acad. Sci. USA 119 (2022), e2201607119.
- [20] Y. Yao, Z. Huang, P. Xie, L. Wu, L. Ma, T. Li, Z. Pang, M. Jiao, Z. Liang, J. Gao, Y. He, D.J. Kline, M.R. Zachariah, C. Wang, J. Lu, T. Wu, T. Li, C. Wang, R. Shahbazian-Yassar, L. Hu, High temperature shockwave stabilized single atoms, Nat. Nanotechnol. 14 (2019) 851–857.

[21] Z. Huang, Y. Yao, Z. Pang, Y. Yuan, T. Li, K. He, X. Hu, J. Cheng, W. Yao, Y. Liu, A. Nie, S. Sharifi-Asl, M. Cheng, B. Song, K. Amine, J. Lu, T. Li, L. Hu, R. Shahbazian-Yassar, Direct observation of the formation and stabilization of metallic nanoparticles on carbon supports, *Nat. Commun.* 11 (2020) 6373.

[22] Y. Yao, Q. Dong, A. Brozena, J. Luo, J. Miao, M. Chi, C. Wang, I.G. Kevrekidis, Z. J. Ren, J. Greeley, G. Wang, A. Anapolksky, L. Hu, High-entropy nanoparticles: synthesis-structure-property relationships and data-driven discovery, *Science* 376 (2022) eabn3103.

[23] J. Huang, A. Jones, T.D. Waite, Y. Chen, X. Huang, K.M. Rosso, A. Kappler, M. Mansor, P.G. Tratnyek, H. Zhang, Fe(II) redox chemistry in the environment, *Chem. Rev.* 121 (2021) 8161–8233.

[24] Y. Liu, J. Qiao, Y. Sun, X. Guan, Simultaneous sequestration of humic acid-complexed Pb(II), Zn(II), Cd(II), and As(V) by sulfidated zero-valent iron: performance and stability of sequestration products, *Environ. Sci. Technol.* 56 (2022) 3127–3137.

[25] M. Li, Y. Mu, H. Shang, C. Mao, S. Cao, Z. Ai, L. Zhang, Phosphate modification enables high efficiency and electron selectivity of nZVI toward Cr(VI) removal, *Appl. Catal. B Environ.* 263 (2020), 118364.

[26] Y. Hu, G. Zhan, X. Peng, X. Liu, Z. Ai, F. Jia, S. Cao, F. Quan, W. Shen, L. Zhang, Enhanced Cr(VI) removal of zero-valent iron with high proton conductive $\text{FeC}_2\text{O}_4\text{-}2\text{H}_2\text{O}$ shell, *Chem. Eng. J.* 389 (2020), 124414.

[27] L. Qian, W. Zhang, J. Yan, L. Han, Y. Chen, D. Ouyang, M. Chen, Nanoscale zero-valent iron supported by biochars produced at different temperatures: synthesis mechanism and effect on Cr(VI) removal, *Environ. Pollut.* 223 (2017) 153–160.

[28] Z. Fan, Q. Zhang, B. Gao, M. Li, C. Liu, Y. Qiu, Removal of hexavalent chromium by biochar supported nZVI composite: batch and fixed-bed column evaluations, mechanisms, and secondary contamination prevention, *Chemosphere* 217 (2019) 85–94.

[29] M.G. Evich, M.J.B. Davis, J.P. McCord, B. Acrey, J.A. Awkerman, D.R.U. Knappe, A.B. Lindstrom, T.F. Speth, C. Tebes-Stevens, M.J. Strynar, Z. Wang, E.J. Weber, W. M. Henderson, J.W. Washington, Per- and polyfluoroalkyl substances in the environment, *Science* 375 (2022) eabg9065.

[30] J. Du, J. Bao, C. Lu, D. Werner, Reductive sequestration of chromate by hierarchical FeS@Fe^0 particles, *Water Res.* 102 (2016) 73–81.

[31] L. Ling, W.X. Zhang, Enrichment and encapsulation of uranium with iron nanoparticle, *J. Am. Chem. Soc.* 137 (2015) 2788–2791.

[32] Y. Mu, Z. Ai, L. Zhang, F. Song, Insight into core-shell dependent anoxic Cr(VI) removal with $\text{Fe}@\text{Fe}_2\text{O}_3$ nanowires: indispensable role of surface bound Fe(II), *ACS Appl. Mater. Interfaces* 7 (2015) 1997–2005.

[33] K.C.K. Lai, I.M.C. Lo, Removal of chromium(VI) by acid-washed zero-valent iron under various groundwater geochemistry conditions, *Environ. Sci. Technol.* 42 (2008) 1238–1244.

[34] S.J. Kim, Y.I. Kim, B. Lamichhane, Y.H. Kim, Y. Lee, C.R. Cho, M. Cheon, J.C. Kim, H.Y. Jeong, T. Ha, J. Kim, Y.H. Lee, S.G. Kim, Y.M. Kim, S.Y. Jeong, Flat-surface-assisted and self-regulated oxidation resistance of Cu(111), *Nature* 603 (2022) 434–438.

[35] K. Chung, J. Bang, A. Thacharon, H.Y. Song, S.H. Kang, W.S. Jang, N. Dhull, D. Thapa, C.M. Ajmal, B. Song, S.G. Lee, Z. Wang, A. Jetbyayeva, S. Hong, K.H. Lee, E.J. Cho, S. Baik, S.H. Oh, Y.M. Kim, Y.H. Lee, S.G. Kim, S.W. Kim, Non-oxidized bare copper nanoparticles with surface excess electrons in air, *Nat. Nanotechnol.* 17 (2022) 285–291.

[36] J.M. Yoo, H. Shin, D.Y. Chung, Y.E. Sung, Carbon shell on active nanocatalyst for stable electrocatalysis, *Acc. Chem. Res.* 55 (2022) 1278–1289.

[37] Y. Liu, J. Luo, L. Tang, C. Feng, J. Wang, Y. Deng, H. Liu, J. Yu, H. Feng, J. Wang, Origin of the enhanced reusability and electron transfer of the carbon-coated Mn_3O_4 nanocube for persulfate activation, *ACS Catal.* 10 (2020) 14857–14870.

[38] D. Wang, N.B. Saleh, A. Byro, R. Zepp, E. Sahle-Demessie, T.P. Luxton, K.T. Ho, R. M. Burgess, M. Flury, J.C. White, C. Su, Nano-enabled pesticides for sustainable agriculture and global food security, *Nat. Nanotechnol.* 17 (2022) 347–360.

[39] Y. Chen, M. Zhang, T. Chen, G. Zhang, H. Xu, H. Sun, L. Zhang, Facile fabrication of rGO/PPy/nZVI catalytic microreactor for ultrafast removal of p-nitrophenol from water, *Appl. Catal. B Environ.* 324 (2023), 122270.

[40] C. Li, Z. Wang, M. Liu, E. Wang, B. Wang, L. Xu, K. Jiang, S. Fan, Y. Sun, J. Li, K. Liu, Ultrafast self-heating synthesis of robust heterogeneous nanocarbides for high current density hydrogen evolution reaction, *Nat. Commun.* 13 (2022) 3338.

[41] Y. Qi, Y. Zhang, L. Yang, Y. Zhao, Y. Zhu, H. Jiang, C. Li, Insights into the activity of nickel boride/nickel heterostructures for efficient methanol electrooxidation, *Nat. Commun.* 13 (2022) 4602.

[42] K. Wei, H. Li, H.Y. Gu, X.F. Liu, C.C. Ling, S.Y. Cao, M.Q. Li, M.Z. Liao, X. Peng, Y. B. Shi, W.J. Shen, C. Liang, Z.H. Ai, L.Z. Zhang, Strained zero-valent iron for highly efficient heavy metal removal, *Adv. Funct. Mater.* 32 (2022), 2200498.

[43] L. Ling, X. Huang, M. Li, W.X. Zhang, Mapping the reactions in a single zero-valent iron nanoparticle, *Environ. Sci. Technol.* (2017) 14293–14300.

[44] D. Zhao, K. Yu, P. Song, W. Feng, B. Hu, W.-C. Cheong, Z. Zhuang, S. Liu, K. Sun, J. Zhang, C. Chen, Atomic-level engineering $\text{Fe}_1\text{N}_2\text{O}_2$ interfacial structure derived from oxygen-abundant metal-organic frameworks to promote electrochemical CO_2 reduction, *Energy Environ. Sci.* 15 (2022) 3795–3804.

[45] M. Jiao, Q. Zhang, C. Ye, Z. Liu, X. Zhong, J. Wang, C. Li, L. Dai, G. Zhou, H. M. Cheng, Recycling spent $\text{LiNi}_{1-x-y}\text{Mn}_x\text{Co}_y\text{O}_2$ cathodes to bifunctional NiMnCo catalysts for zinc-air batteries, *Proc. Natl. Acad. Sci. USA* 119 (2022) e2202202119.

[46] W.A. Algozeeb, P.E. Savas, D.X. Luong, W. Chen, C. Kittrell, M. Bhat, R. Shahsavari, J.M. Tour, Flash graphene from plastic waste, *ACS Nano* 14 (2020) 15595–15604.

[47] B. Culp, CRC Handbook of Chemistry and Physics 2000–2001, Library Journal, New York Library Journals, New York, 2000.

[48] F. Yu, C. Jia, X. Wu, L. Sun, Z. Shi, T. Teng, L. Lin, Z. He, J. Gao, S. Zhang, L. Wang, S. Wang, X. Zhu, Rapid self-heating synthesis of Fe-based nanomaterial catalyst for advanced oxidation, *Nat. Commun.* 14 (2023) 4975.

[49] A.F. White, M.L. Peterson, Reduction of aqueous transition metal species on the surfaces of Fe(II) -containing oxides, *Geochim. Cosmochim. Acta* 60 (1996) 3799–3814.

[50] R. Gao, L. Xu, M. Sun, M. Xu, C. Hao, X. Guo, F.M. Colombari, X. Zheng, P. Král, A. F. de Moura, C. Xu, J. Yang, N.A. Kotov, H. Kuang, Site-selective proteolytic cleavage of plant viruses by photoactive chiral nanoparticles, *Nat. Catal.* 5 (2022) 694–707.

[51] A. Palika, A. Armanious, A. Rahimi, C. Medaglia, M. Gasbarri, S. Handschin, A. Rossi, M.O. Pohl, I. Busnadio, C. Gubeli, R.B. Anjanappa, S. Bolisetty, M. Peydayesh, S. Stertz, B.G. Hale, C. Tapparel, F. Stellacci, R. Mezzenga, An antiviral trap made of protein nanofibrils and iron oxyhydroxide nanoparticles, *Nat. Nanotechnol.* 16 (2021) 918–925.